



**HAL**  
open science

## AgxCu100-x decorated Si micropillars as photocathodes for the reduction of CO<sub>2</sub>

Harsh Chaliyawala, Stéphane Bastide, Christine Cachet-vivier, Nikola Ilic,  
Tarik Bourouina, Frédéric Marty, Kadiatou Bah, E. Torralba

► **To cite this version:**

Harsh Chaliyawala, Stéphane Bastide, Christine Cachet-vivier, Nikola Ilic, Tarik Bourouina, et al..  
AgxCu100-x decorated Si micropillars as photocathodes for the reduction of CO<sub>2</sub>. 2024. hal-04766197

**HAL Id: hal-04766197**

**<https://hal.science/hal-04766197v1>**

Preprint submitted on 4 Nov 2024

**HAL** is a multi-disciplinary open access archive for the deposit and dissemination of scientific research documents, whether they are published or not. The documents may come from teaching and research institutions in France or abroad, or from public or private research centers.

L'archive ouverte pluridisciplinaire **HAL**, est destinée au dépôt et à la diffusion de documents scientifiques de niveau recherche, publiés ou non, émanant des établissements d'enseignement et de recherche français ou étrangers, des laboratoires publics ou privés.

# **Ag<sub>x</sub>Cu<sub>100-x</sub> decorated Si micropillars as photocathodes for the reduction of CO<sub>2</sub>**

*Harsh Chaliyawala<sup>1</sup>, Stephane Bastide<sup>\*1</sup>, Christine Cachet-Vivier<sup>1</sup>, Nikola Ilic<sup>1</sup>, Tarik Bourouina<sup>2</sup>, Frédéric Marty<sup>2</sup>, Kadiatou Bah<sup>1</sup>, Encarnacion Torralba<sup>1\*</sup>*

<sup>1</sup> Univ Paris Est Creteil, CNRS, ICMPE, UMR 7182, 2 rue Henri Dunant, 94320 Thiais, France

<sup>2</sup> Université Gustave Eiffel, ESYCOM, CNRS UMR 9007, ESIEE Paris, Noisy-le-Grand, France

This work reports the fabrication of *p*-type Si micropillar (MP) substrates decorated with Ag<sub>x</sub>Cu<sub>100-x</sub> bimetallic nanoparticles and their application as photocathodes for CO<sub>2</sub> photoelectrochemical reduction. Metal deposition by metal-assisted chemical etching is chosen as the nanoparticle synthesis method, to explore for the first time its capabilities for 3D structures. It is found to be applicable, allowing a good control of the composition, with nanoparticles distributed along the entire MP, but with a coverage gradient from top to bottom. The Ag<sub>x</sub>Cu<sub>100-x</sub> decorated Si MPs photocathodes show enhanced light trapping compared to flat Si, with 45 % lower reflectance values in the visible and significantly higher catalytic activity, in terms of photocurrent density, overpotential and power savings (4.7 % for Ag<sub>50</sub>Cu<sub>50</sub>/Si MPs *vs.* 3% for Ag<sub>50</sub>Cu<sub>50</sub>/flat-Si). Si MPs coated with Ag<sub>50</sub>Cu<sub>50</sub> and Ag<sub>20</sub>Cu<sub>80</sub> provide the highest gain in potential (440 and 600 mV *vs.* bare Si MPs) and an increased selectivity towards high energy density products (*i.e.*, CH<sub>4</sub>) compared to monometallic photocathodes. These are promising features for efficient light-driven CO<sub>2</sub> conversion. However, a significant metal loss is observed during photoelectrolysis, especially for Cu-rich compositions. Suggestions to improve the photocathode performance in terms of metal coating homogeneity and catalyst stability are presented.

---

\* Corresponding Authors: [encarnacion.torralba-penalver@cnrs.fr](mailto:encarnacion.torralba-penalver@cnrs.fr), [stephane.bastide@cnrs.fr](mailto:stephane.bastide@cnrs.fr)

## 1 Introduction

The impact of CO<sub>2</sub> emissions on global warming creates an urgent need for clean and alternative sources (*e.g.*, solar, hydrothermal and wind) for energy storage and generation that can overcome the challenges of climate change<sup>[1,2]</sup>. Artificial photosynthesis is a promising research area for energy storage. The term applies to artificial devices that convert solar energy into fuels (*i.e.*, solar-to-chemical energy conversion) by using photogenerated charge carriers to drive the chemical reactions<sup>[3-7]</sup>. Various semiconductors (SCs)-based technologies for H<sub>2</sub> production from water splitting and low-carbon fuel production from CO<sub>2</sub> reduction have been studied to mimic the photosynthesis effect (*i.e.*, artificial leaves<sup>[5]</sup>, SC-based photocatalytic<sup>[6,7]</sup> and photoelectrocatalytic<sup>[3,4]</sup> systems). The photoelectrochemical CO<sub>2</sub> reduction reaction (PEC-CO<sub>2</sub>RR) using SCs as photocathodes is attracting increasing interest. By utilizing solar radiation as a renewable energy input and the appropriate catalyst, PEC-CO<sub>2</sub>RR can convert harmful anthropogenic CO<sub>2</sub> to low-carbon fuels (also called solar fuels) and valuable everyday products, that can be readily utilized in the existing infrastructures<sup>[8,9]</sup>. Silicon (Si) is regarded as a promising photocathode material due to its large abundance, low cost, and promising electrical and optical properties<sup>[10-13]</sup>. Several strategies to improve the overpotential and the selectivity of Si substrates for CO<sub>2</sub> reduction by the addition of appropriate metal catalyst (*e.g.*, Ag, Cu or Au) have been reported using various methods, including photoelectrodeposition, atomic layer deposition (ALD), *sputtering*, etc.<sup>[14]</sup> The incorporation of metal nanoparticles (NPs) on the Si supports favors the collection of photogenerated carriers without preventing light from reaching the semiconductor, allowing significant photocurrent densities at low overpotentials for PEC-CO<sub>2</sub>RR<sup>[13,14]</sup>.

Bimetallic catalysts have been applied to boost the CO<sub>2</sub>RR performances in terms of structural stability, selectivity and activity<sup>[15]</sup>. This is due to their tunable composition and crystalline structure, which provide new active sites with optimized binding strengths for targeted catalytic reactions<sup>[16]</sup>. Various bimetallic catalysts for CO<sub>2</sub>RR have been reported for a variety of products, particularly Cu-based bimetallic catalysts<sup>[15,17,18]</sup>. Despite their interest, the combination of Cu-based bimetallic NPs with Si photoactive supports is still quite unexplored. In a recent publication we proposed an original method based on Metal-Assisted Chemical Etching (MACE) of Si to deposit bimetallic Ag<sub>x</sub>Cu<sub>100-x</sub> NPs on planar Si substrates, and we applied these materials as photocathodes for PEC-CO<sub>2</sub>RR for the first time<sup>[19]</sup>. The

system provided encouraging results in terms of photocatalytic activity and selectivity over monometallic photocathodes. Thus, a shift in the onset potential of 840 mV was observed for Ag<sub>50</sub>Cu<sub>50</sub>/p-Si with respect to an analogous metal electrode in a CO<sub>2</sub>-saturated 0.5 mol L<sup>-1</sup> NaHCO<sub>3</sub> aqueous solution, with c.a. 3% of power saving<sup>[19]</sup>. The bimetallic nanoparticles enhanced the selectivity towards the production of high energy density products. Thus, maximum Faradaic efficiencies of 26% and 18.2% were obtained for the production of CH<sub>4</sub> and CO, at potentials of - 0.72 V and - 0.87 V vs. RHE, respectively. Recently, we have extended our deposition method to the Cu-Pd system with interesting results<sup>[20]</sup>.

For large-scale applications, three-dimensional (3D) photocathodes are required. In this sense, 3D electrodes based on Si micropillars (Si MPs) can offer several advantages for PEC reactions: (i) increased contact surface area with the electrolyte (vs. flat Si), (ii) higher catalytic loading than for flat surfaces, and (iii) enhanced light absorption, implying more effective separation and collection of photocarriers<sup>[21-23]</sup>. In this line, the combination of Si MPs with nanoelectrocatalysts shows great potential for solar energy conversion<sup>[23]</sup>. In 2020, Kempler et. al first reported the use of metal-decorated Si MPs for PEC-CO<sub>2</sub>RR. They demonstrated that arrays of short, sparse microwires (diameter, pitch, and height of 3, 7, and 30 μm, respectively) with a pn<sup>+</sup> radial junction, can accommodate sufficient Cu loading on the illuminated side (*i.e.*, without reflectivity losses thanks to the microwire geometry) to match the j-E behavior of pure Cu (similar mixture of C1-C3 products, FE of 20% for CH<sub>4</sub> + C<sub>2</sub>H<sub>4</sub> at 0.45 V vs. RHE)<sup>[24]</sup>. A photocurrent density of 25 mA/cm<sup>2</sup> at -0.5 V vs. RHE was achieved and maintained for 48h. These initial results demonstrate the feasibility and real-world application of Si MPs based photocathodes for PEC-CO<sub>2</sub>RR. However, more than 90% of the photocurrents (48 h) result from the hydrogen evolution reaction (HER) with a faradaic efficiency of CH<sub>4</sub> + C<sub>2</sub>H<sub>4</sub> of only ~ 3%, which seems to be related to the aggregation and delamination of the deposited Cu, leaving bare Si surfaces favorable for HER.

Two main factors are identified as sources of instability of Cu-based electrodes: (i) structural reorganization and (ii) degradation under CO<sub>2</sub>RR conditions<sup>[25,26]</sup>. In the particular case of Si photocathodes, poor adhesion of Cu to Si and photo-corrosion are additional sources of degradation<sup>[13,27]</sup>. Developing protective layers or depositing co-catalyst by different techniques are among the strategies being studied for increasing photocathode stability<sup>[13,14]</sup>. In this line Cu-based bimetallic materials are an encouraging choice, because of their recognise capabilities of preventing Cu reorganization and tuning the selectivity<sup>[17,18]</sup>.

In the present work, we investigate the compatibility of bimetallic deposition by MACE with three-dimensional (3D) structures, specifically Si MPs, and we test the resulting photocathodes for PEC-CO<sub>2</sub>RR. Ag<sub>x</sub>Cu<sub>100-x</sub> is chosen as the bimetallic system for its intrinsic interest <sup>[15]</sup> and for the sake of comparison with results obtained on flat substrates <sup>[19]</sup>. Si MPs with different dimensions (pitch, height, and side) are considered.

## 2 Experimental procedure

### 2.1 Materials and Reagents

30 wt% Ag(NO<sub>3</sub>) (99.8 wt% Ag) and Cu(SO<sub>4</sub>)·5H<sub>2</sub>O (98.5 wt% Cu) from VWR-Prolabo were used as metal precursors for Si metallization. HF 40% (d = 1.13 kg/L, VWR) was used for Si cleaning (*i.e.*, native oxide removal) and as co-reactant for Si metallization. Dilution and cleaning were performed with 18.2 MΩ·cm ultra-pure water (Millipore). [Ru(NH<sub>3</sub>)<sub>6</sub>]Cl<sub>3</sub> (Sigma-Aldrich) was used as redox probe.

### 2.2 Fabrication of Si MPs

The micropillars (MPs) have been fabricated on a double-side polished 525 μm thick 4 inch Si wafer. The wafer is first thermally oxidized to form a 1 μm thick SiO<sub>2</sub> layer, which serves as a mask for the deep reactive ion etching (DRIE) of Si. Next, a 1.1 μm thick layer of JSR PFR 7790G photoresist (PR) is spin-coated over the SiO<sub>2</sub> layer and photolithographically patterned to define the shape of the PR. The oxide layer is then etched in a plasma reactor, followed by photoresist removal in acetone. The next step is the Si etch, which is performed in an ALCATEL A601E DRIE reactor. The etching process employs a ‘Bosch process’ alternating between etching and sidewall passivation steps using SF<sub>6</sub> gas for 5 seconds and C<sub>4</sub>F<sub>8</sub> gas for 2 seconds, respectively. The passivation step protects the etched sidewalls to prevent lateral etching, enabling the formation of high aspect ratio structures. The MPs were etched to a depths of ~60 μm and ~120 μm. The wafer then underwent O<sub>2</sub> plasma cleaning to remove the passivation layer on the sidewalls. The final step is a HF wet etch of the remaining SiO<sub>2</sub> in HF. Square and cylindrical MPs with different dimensions in terms of pitch or interpillar distance (P), pillar side or diameter (A) and pillar height (H) were used. Specifically, MPs arrays with P = 20, 50, and 100 μm, A = 2, 5, and 10 μm, and H = 60 and 120 μm, were fabricated.

**Figure 1a** shows a Si wafer with 9 photoelectrodes with Si MPs patterned according to the above fabrication processes. The MPs are located on the spherical dark regions (1.5 cm diameter) in the center of each pre-cut Si photoelectrode (square of 2 cm side). Figure S1 in the Supporting Information (SI) shows a more detailed scheme of the patterned Si wafer, along with additional SEM images of the Si MPs. Si samples of 2x2 cm<sup>2</sup> with cylindrical MPs were used for reflectivity measurements and long-term chronoamperometry (sections 3.3 and 3.7). Smaller photoelectrodes (patterned region of 0.5 cm diameter) were used for metal deposition tests (section 3.2) and CV analysis (section 3.4 and 3.6). Square and cylindrical MPs with different A-values were used indistinguishably for the metal deposition tests. The remaining characterizations and measurements from Section 3.3 and onward, were performed with cylindrical MPs of A = 10 μm, P = 20 μm, and H = 60 μm.

When necessary, comparative experiments on flat Si substrates were performed with P-type boron doped (100) c-Si polished wafers ( $\rho = 1\text{-}3\text{ ohm cm}$ ,  $500\pm 25\text{ }\mu\text{m}$  thick) purchased from Sievert Wafer.

### 2.3 Synthesis of Ag<sub>x</sub>Cu<sub>100-x</sub> NPs on Si MPs

Ag, Cu and Ag<sub>x</sub>Cu<sub>100-x</sub> NPs with targeted x values of 20, 40, 50 and 80 were synthesized on the Si MPs substrates by bimetallic MACE deposition, by following the protocol developed in <sup>[19]</sup>. Prior to metal deposition, the Si MPs were immersed in 0.1 mol L<sup>-1</sup> HF solution for few minutes to remove the native SiO<sub>2</sub> layer. No additional cleaning treatment (*e.g.*, piranha) was used because the Si wafers were pre-cut and pre-cleaned in the clean room prior to fabrication of the Si MPs. Metallization was performed by immersing the Si MPs substrate in the precursor's solution (30 ml of 0.1 mol L<sup>-1</sup> HF solution containing Ag<sup>+</sup> and Cu<sup>2+</sup> ions at concentrations adjusted according to the target atomic composition <sup>[19]</sup>), followed by extensive rinsing with ultrapure water and drying with a stream of compressed dinitrogen (N<sub>2</sub>). Bimetallic deposition by MACE enables the in-situ generation of bimetallic NPs on the Si substrate surface at room temperature, without the need for an external electrical circuit. It also allows for optimal contact between the NPs and the Si due to the absence of surface oxides, and it is easily scalable. **Figure 1b** shows a schematic view of a cylindrical MP, bare and modified with Ag<sub>x</sub>Cu<sub>100-x</sub> NPs.

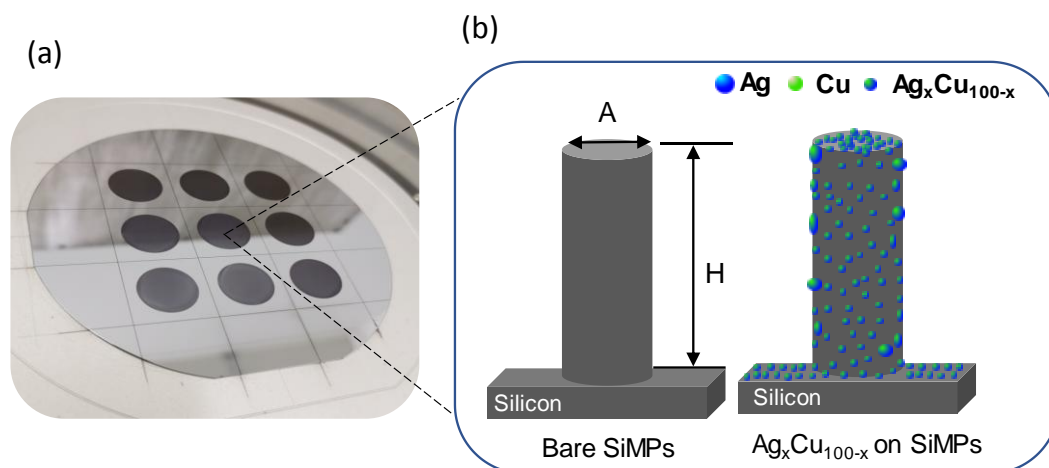


Figure 1. (a) Optical image of patterned Si MPs on a p-type Si wafer. Pre-cut lines define the electrodes with a final size of  $2 \times 2 \text{ cm}^2$ . The diameter of the MP region is  $\phi=15 \text{ mm}$ . (b) Schematic of a Si MP, bare (left) and decorated with  $\text{Ag}_x\text{Cu}_{100-x}$  NPs (right), where A is the MP diameter and H the MP height. The MP pitch, or pillar inter-distance (not presented on the figure) is indicated by P through the text.

## 2.4 Material Characterization

Morphology and elemental composition (bulk properties) were analyzed by field emission scanning electron microscopy (FESEM) coupled with energy dispersive X-ray analysis (SEM-EDX) using a Zeiss Merlin FEG microscope equipped with an Aztec EDS Advanced system (HKL Nordlys Nano, Oxford Instruments) and an X-Max SDD detector. Chemical states and surface elemental composition were analyzed by K-alpha X-ray photoelectron spectroscopy (XPS) equipped with an ion beam etcher from Thermo Fisher Scientific. Microstructural observations were performed by transmission electron microscopy (TEM) using a 200 kV FEG TEM (FEI Tecnai F20 equipped with a Gatan CCD camera Orius 1000, point-to-point resolution 0.24 nm), and the chemical analysis is performed on the same microscope with an EDX windowless detector ( $60 \text{ mm}^2$ ). For TEM observations, NPs were collected on Au mesh grids by pouring a few drops of ethanol solutions in which the Si MPs/ $\text{Ag}_x\text{Cu}_{100-x}$  samples were previously sonicated.

## 2.5 Electrochemical measurements

A homemade O-ring type three-electrode PEC cell (volume of 54 mL) equipped with a quartz window was used for the electrochemical measurements <sup>[19]</sup>. It was coupled to a Metrohm Autolab PGSTAT 30 potentiostat equipped with NOVA software. The working electrode was the metallized p-Si MPs, the counter electrode was a Pt plate, and the reference electrode was  $\text{Ag}/\text{AgCl}/3 \text{ mol L}^{-1} \text{ KCl}$  ( $0.209 \text{ V vs. NHE}$ ). All potentials were converted to

the RHE reference scale unless otherwise noted ( $E_{vs. RHE} = E_{vs. Ag/AgCl} + 0.209 + 0.059 \text{ pH}$ ). The electrocatalytic reduction of  $\text{CO}_2$  was performed in  $0.5 \text{ mol L}^{-1} \text{ NaHCO}_3$  at room temperature ( $\text{pH} = 8.4$ ). Prior to the experiment, 36 mL of electrolyte were added to the cell and purged with Ar for 10 min ( $\text{pH} = 8$ ). The electrolyte was then bubbled with  $\text{CO}_2$  (Alphagaz N45) for 20 min to ensure  $\text{CO}_2$  saturation ( $\text{pH} \sim 7.4$ ,  $[\text{CO}_2] = 33 \text{ mmol L}^{-1}$ ). The  $\text{CO}_2$  atmosphere was maintained throughout the experiment. The illuminated MPs area was  $1.77 \text{ cm}^2$  (O-ring inner diameter = 15 mm). Cyclic voltammetry was used as the electrochemical characterization technique and chronoamperometry was used for long-term electrolysis. The illumination source was a Newport LSH7320 solar simulator providing AM1.5G light with a power of  $1000 \text{ Wm}^{-2}$ . Polished Ag and Cu plates were used as reference conductor electrodes. Before each electrochemical measurement they were polished with alumina powder (1 and  $0.3 \mu\text{m}$ ) and washed thoroughly with ultrapure water. The Cu plate was additionally immersed in HCl/water (50:50 v/v) for oxide removal.

## 2.6 Product analysis

The gas products were analyzed by gas chromatography (GC). A Shimadzu gas chromatograph (GC 2010 Pro) equipped with a barrier ionization detector (BID 2010 plus) and a micropacked ShinCarbon GC column was used to analyze the gas composition inside the electrochemical cell during the bulk electrolysis. The gas was manually sampled from the electrochemical cell and injected into the GC at regular 10-min intervals during the electrolysis. An etalon gas mixture purchased from Air Liquide was used to calculate the concentration of the gases produced. He was used as carrier gas.

# 3 Result and Discussion

## 3.1 Effect of the Si MPs geometrical characteristics on the PEC response

To investigate the influence of the MP geometry on the electrochemical response compared to a polished surface, we performed CV measurements with a typical reversible redox probe, the  $\text{Ru}(\text{NH}_3)_6^{3+}/\text{Ru}(\text{NH}_3)_6^{2+}$  couple. The comparison of the CV response of a flat Si photocathode and a typical metal electrode (Pt disk) in the presence of  $\text{Ru}(\text{NH}_3)_6^{3+}$  is shown in Figure S2 of the SI. Essentially, the signal from the semiconductor is distorted (larger separation between peaks) compared to a metallic conductor, due to sluggish electron transfer kinetics. Interestingly, two reduction peaks instead of one are observed in the cathodic scan. A study of  $\ln(I_{peak})$  vs.  $\ln(\nu)$  gave a slope of 0.5 for both reduction peaks, which

indicate that the second peak is not related to adsorptive interactions. A possible explanation could be the reduction of an ion pair formed between  $\text{Ru}(\text{NH}_3)_6^{3+}$  and  $\text{K}_2\text{SO}_4$  [28]. Despite these discrepancies, this redox probe remains suitable for the evaluation of the geometrical characteristics of the Si MPs vs. polished Si.

**Figure 2** shows the CV curves obtained with Si MPs substrates with different values of pitch and height (**Figure 2a** and **b**, respectively) at 0.2 sun illumination (*i.e.*,  $20 \text{ mW cm}^{-2}$ ) in a  $5 \text{ mmol L}^{-1} \text{ Ru}(\text{NH}_3)_6^{3+}$  solution with  $0.5 \text{ mol L}^{-1} \text{ K}_2\text{SO}_4$ . Focusing on the interpillar distance P for a given MP height (**Figure 2a**), an increase in the peak current density with decreasing P can be observed (more easily in the oxidation region), with the lowest peak current supplied by the flat electrode (black curve). This behavior can be related to the developed surface area, since it increases with decreasing pitch (see Table S1 in the SI for the developed surface area in each case). As shown in Figure S3 in the SI, a plot of the normalized peak current ( $I_{peak}$ ) as a function of the developed surface area (decreasing P) deviates from the expected linear dependence on diffusion according to the Randles-Sevcik model. This may indicate a mixed contribution to the current response from thin film (interpillar volume) and diffusion behavior [29], which justifies the cathodic and anodic peaks moving closer together as P decreases (**Figure 2a**).

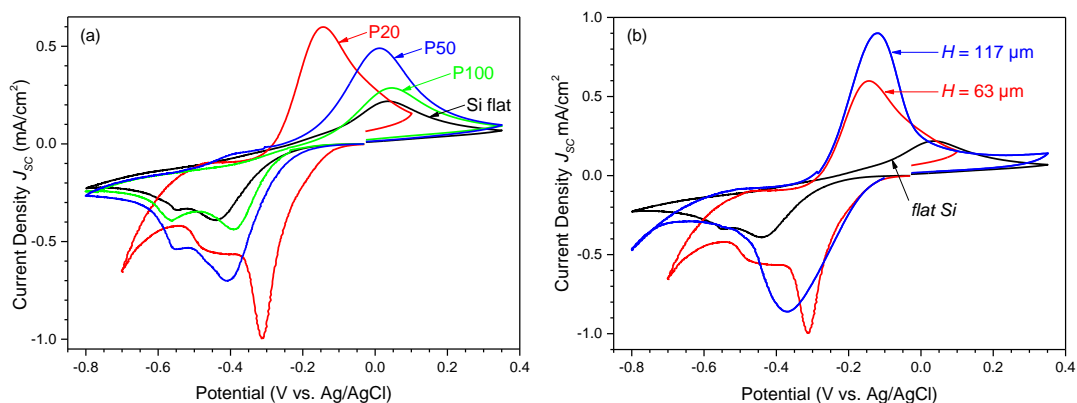


Figure 2. Cyclic voltammetry performed on samples with various (a) Pitch ( $P = 20, 50, 100 \mu\text{m}$ ) and (b) Height ( $H = \sim 63$  and  $\sim 117 \mu\text{m}$ ). Electrolyte:  $\text{K}_2\text{SO}_4$  at  $0.5 \text{ mol L}^{-1}$  and  $\text{Ru}(\text{NH}_3)_6\text{Cl}_3$  at  $0.005 \text{ mol L}^{-1}$ , under Ar. Illumination :  $0.2 \text{ sun}$  ( $20 \text{ mW cm}^{-2}$ ). Current density vs. the geometric area ( $0.196 \text{ cm}^2$ ).

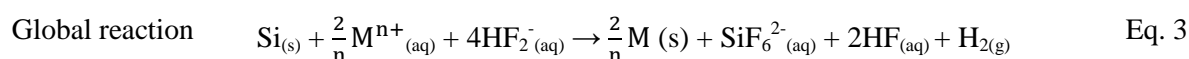
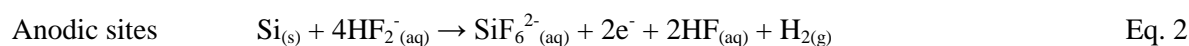
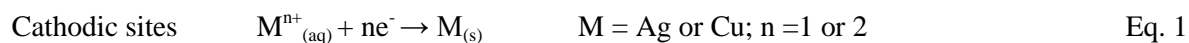
**Figure 2b** compares the CVs of two samples of Si MPs with the same interpillar distance ( $20 \mu\text{m}$ ), but different heights ( $117$  vs.  $63 \mu\text{m}$ ). The current peaks appear to be approximately at the same potentials. However, there is a discrepancy between the reduction

and oxidation regimes in terms of peak heights. In the cathodic region, the peak for the long MPs is broader and not well defined, and therefore less intense than that for the small MPs. On the contrary, it is almost two times higher in the anodic region, indicating that a much larger quantity of  $\text{Ru}(\text{NH}_3)_6^{3+}$  is indeed reduced during the cathodic scan.

The MPs with the smaller pitch and longer height appeared to be the most promising for the PEC tests. However, we found that they are also more fragile and break relatively easily during HER. Therefore, we selected MPs with a pitch of 20  $\mu\text{m}$  and a height of 60  $\mu\text{m}$  for the PEC tests.

### 3.2 Bimetallic deposition by MACE on Si MPs

Si MPs were metallized by immersion in a HF solution containing the two ionic metal precursors (see experimental section 2.3 for more details). Briefly, when  $\text{Ag}^+$  and/or  $\text{Cu}^{2+}$  ions get in contact with the Si surface, they are spontaneously reduced (Eq. 1) and become catalytic sites for subsequent ion reduction and NP growth. At the same time, Si atoms in the vicinity of the metal ions are oxidized to supply the necessary electrons. In HF media, Si dissolution occurs in the porous Si formation regime (Eq. 2). The chemical reactions involved are:



In accordance with the number of electrons exchanged for the reduction of  $\text{Cu}^{2+}$  ( $2\text{e}^-$ ) and  $\text{Ag}^+$  ( $1\text{e}^-$ ), Cu is deposited at a rate two times lower than Ag. The  $[\text{Cu}^{2+}]/[\text{Ag}^+]$  ratio should therefore be twice that of the desired  $\text{Ag}_x\text{Cu}_{100-x}$  composition, *i.e.*,  $2(100-x)/x$ . (21). For example, the Cu and Ag salt precursors are 2 and 1  $\text{mmol L}^{-1}$ , respectively, to deposit  $\text{Ag}_{50}\text{Cu}_{50}$ .

**Figure 3** shows representative SEM images of cylindrical Si MPs P20A10, bare (a-c) and decorated with  $\text{Ag}_{50}\text{Cu}_{50}$  bimetallic NPs deposited by MACE (d-f). Figure S4 in the SI gives additional SEM images for the deposition of pure metals and other bimetallic compositions. The Si MPs exhibit a peculiar wave-like structure (rings easily visible on the bare samples, **Figure 3a-c**). This is due to the clean room fabrication process, which includes multiple etching and passivation cycles to shape the sample.

The images show a gradient in metal deposition from the top (high) to the bottom (low), with at the top the formation of dendrites and along the MP a decreasing NP density. The NP morphology of the Ag<sub>50</sub>Cu<sub>50</sub> deposits is similar to that obtained on planar Si, as reported in <sup>[19]</sup>, *i.e.*, spherical NPs for pure Ag and Cu, and elongated NPs, more densely distributed for the bimetallics. Metal deposition is observed along the entire MP surface (**Figure 3d-f**), with a higher density of NPs deposited at the edges of the wave-like structures (see also **Figure 4**).

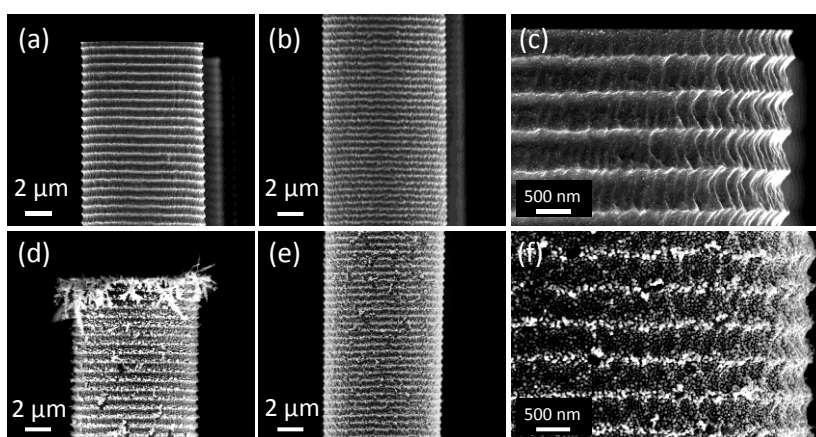


Figure 3. (a) Cross-sectional SEM images showing (a-c) bare Si MPs and (d-f) Si MPs decorated with Ag<sub>50</sub>Cu<sub>50</sub> NPs. Deposition conditions: [Ag<sup>+</sup>] and [Cu<sup>2+</sup>] = 1 and 2 mmol L<sup>-1</sup>, [HF] = 0.1 mmol L<sup>-1</sup>, deposition time = 1 min.

NP nucleation and growth is generally enhanced at sharp edges and irregularities (*e.g.*, higher density of NPs on the MP rings). In addition, a more significant cation supply is possible at the tops of the MPs which are in contact with the bulk of the solution, and this must be the reason for the gradient of NP density along the MPs (diffusion limitation) and for the presence of dendrites only at the tops of the MPs. Dendrite formation and NP density logically increase with time.

To evaluate the homogeneity in bimetallic composition along the MPs, further elemental composition analysis was performed by EDX in different regions of the MPs (top, middle, and bottom) and for deposition times of 1, 2, and 5 minutes (**Figure 4**).

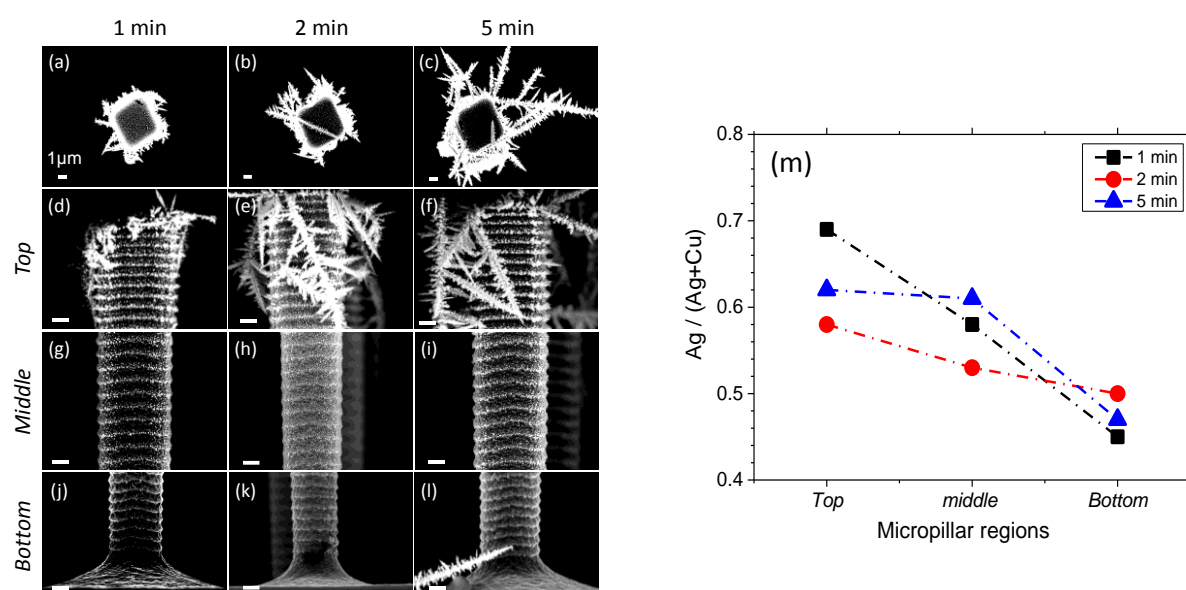


Figure 4. Plan view (a-c) and cross section (d-l) images of  $\text{Ag}_{50}\text{Cu}_{50}$  deposited on Si MPs for 1, 2 and 5 min; (m) Ag fraction of the NPs measured along the MPs for the 3 deposition times.

The atomic composition in the top, middle and bottom regions of the MPs is plotted in **Figure 4m**. While the NP composition at the bottom of the MPs is close to the  $\text{Ag}_{50}\text{Cu}_{50}$  target value, a systematic increase of Ag is observed in the middle and top regions (up to  $\text{Ag}_{70}\text{Cu}_{30}$ ). EDX analysis shows that the dendrites have a Ag fraction of about 66-70% (see Fig. S5 in the SI). This is also in agreement with HAADF-STEM observations (see Fig. S7 in the SI). Note that the surface of the NPs (top  $\sim 1$  nm) can be richer in Ag compared to the bulk values, as observed by XPS analysis in a previous study realized on flat Si substrates under the same metallization conditions <sup>[19]</sup>. For example, NPs with bulk compositions (SEM-EDX) of  $\text{Ag}_{51}\text{Cu}_{49}$  and  $\text{Ag}_{63}\text{Cu}_{37}$  showed a surface with  $\text{Ag}_{60}\text{Cu}_{40}$  and  $\text{Ag}_{68}\text{Cu}_{32}$ , respectively.

Overall, these images demonstrate that bimetallic deposition by MACE is applicable to 3D structures. For Si MPs, a relatively good control of the NP composition is obtained, with NPs distributed with a density gradient from top to bottom. For electrochemical experiments, 1 min deposition was selected to minimize dendrite formation. Nevertheless, we observed during PEC experiments that gas evolution easily detaches the dendrites.

Since dendrite formation and the inhomogeneities in composition and NP density are related to diffusion effects, better overall results can be expected by minimizing the role of diffusion (forced convection, higher concentration). Current studies focus on the investigation of bimetallic deposition under dynamic conditions.

In terms of crystallographic structure, the AgCu NPs synthesized by MACE have a phase separated nature with Ag and Cu nanograins highly intermixed, as shown in our previous work where further morphological and structural characterizations can be found <sup>[19]</sup>. Figure S6 in the SI shows XRD diffractograms of pure Ag, Cu and  $\text{Ag}_{50}\text{Cu}_{50}$  as representative example. The elemental distribution of Ag and Cu in  $\text{Ag}_{50}\text{Cu}_{50}$  and  $\text{Ag}_{20}\text{Cu}_{80}$  NPs observed by STEM-EDX is provided in figure S7, to show the high degree of miscibility of the two elements.

### 3.3 Reflectivity measurement of $\text{Ag}_x\text{Cu}_{100-x}$ bimetallic NPs on planar Si and Si MPs

The reflectance of flat Si and Si MPs, bare or decorated with  $\text{Ag}_x\text{Cu}_{100-x}$  of different compositions, is plotted in **Figure 5**. The reflectance of flat Si is characterized by (i) peaks at 255 nm and 354 nm corresponding to direct band gaps, (ii) decreasing values in the Vis-NIR region (from 400 to 900 nm) determined by the change in refractive index and the front surface properties, (iii) increasing values (from 900 to 1150 nm) when the absorption

coefficient of Si becomes zero (indirect band gap at 1100 nm) and light reflected at the back surface of the sample is also measured. Metallized samples with Ag and Cu NPs exhibit similar reflectance in the visible region, except for a peak at 450 nm in the case of Ag. The lower reflectance observed for  $\text{Ag}_{50}\text{Cu}_{50}/\text{Si}$  in the UV-blue region of the spectrum may be due to plasmonic properties of the NPs in this composition, which either absorb light significantly or promote better light coupling into Si.

The reflectance is lower for all the samples covered with Si MPs (**Figure 5b**). Comparing non-metallized flat Si and Si MPs, the latter have a lower reflectance at 600 nm (18 vs. 35%, respectively). This is due to light scattering induced by the MPs, resulting in multiple bounces of light between them, especially after reflection on the Si substrate (flat areas between the MPs). The remaining reflectivity is probably due to the flat top of the MPs.

Metal deposition on Si MPs slightly increases the reflectance, especially in the case of  $\text{Ag}_{50}\text{Cu}_{50}$  (+4.5 % in a. v. at 600 nm). The intrinsic higher reflectivity of metals and the dendrites formed at the top of the MPs explain this increase. In the case of Ag/Si MPs, there is also a specific peak in the reflectance spectrum (at 500 nm), but it is broader and less intense than for Ag/Si. Contrary to the study of Pana et al. (2022), we do not observe well-defined peaks characterizing the presence of Cu NPs<sup>[30]</sup>. This is probably due to the low amount of Cu deposited on the surface of our samples.

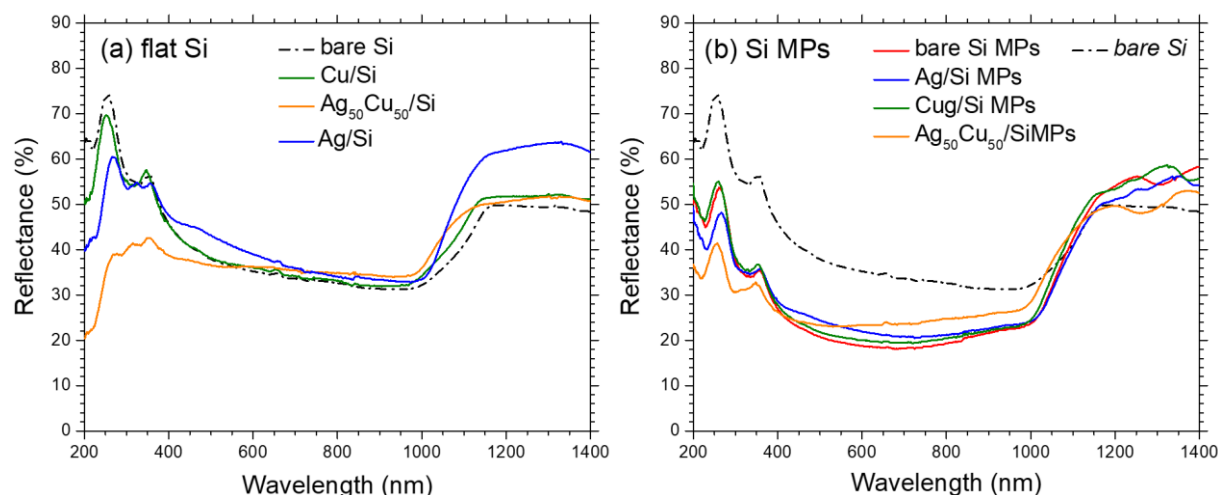


Figure 5. Reflectance from 200-1400 nm of (a) flat Si and (b) Si MPs, bare or decorated with  $\text{Ag}_{50}\text{Cu}_{50}$  NPs. In (b) flat Si is also shown for comparison.

These optical properties imply that the presence of Si MPs on the surface reduces the reflectance even after metallization. We therefore expect higher photocurrents with Si MPs than with flat Si when these samples are used as photoelectrodes.

### 3.4 Comparison of the PEC response of Si MPs/Ag<sub>x</sub>Cu<sub>100-x</sub> vs. Si/Ag<sub>x</sub>Cu<sub>100-x</sub>

**Figure 6** compares the PEC  $j/E$  responses of 3D photoelectrodes decorated with Ag, Cu, and Ag<sub>50</sub>Cu<sub>50</sub> NPs with those of equivalent flat photocathodes for the light-driven CO<sub>2</sub> reduction at 0.2 sun. This illumination level was selected for comparison purposes so that the currents were not strongly affected by the noise induced by gas evolution (see the noise on the CVs recorded at 1sun in figure S8 of the SI). However, for quantitative purposes, *i.e.*, electrolysis coupled to product analysis shown in section 3.7, 1 sun illumination was used. All the voltammograms show similar shape, where the photocurrent increases during the cathodic scan until a photocurrent plateau determined by the photon flux is reached, when all the photocarriers are collected and transferred to the electrolyte. Additional information on the general characteristics of the PEC responses can be found in the literature <sup>[31],[32,33]</sup>.

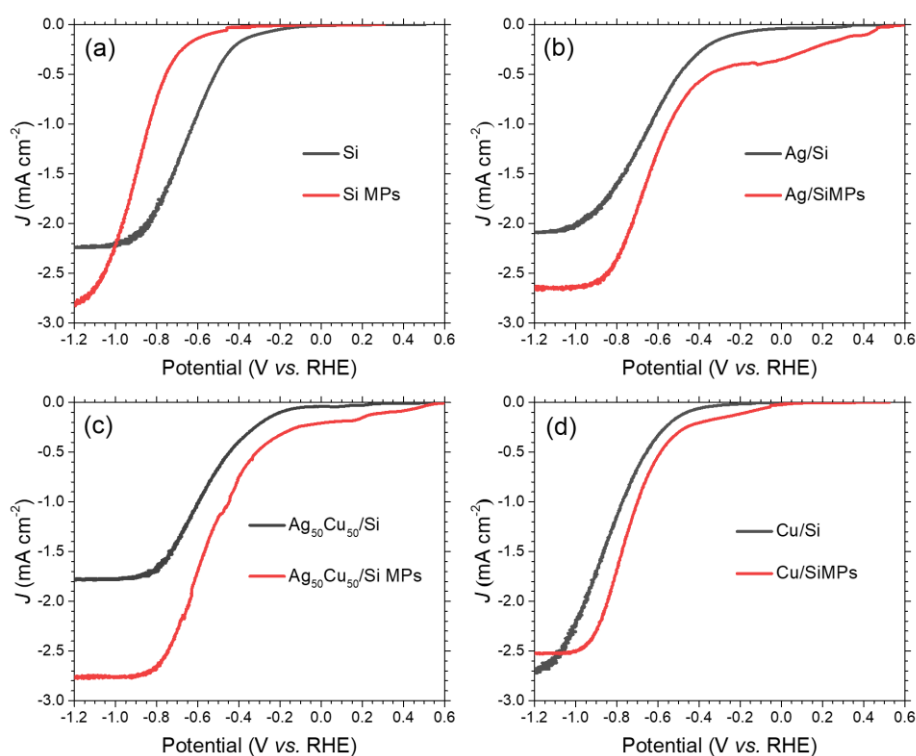


Figure 6. PEC responses obtained under 0.2 sun illumination with (a) bare Si and Si MPs; (b) Ag/Si and Ag/Si MPs; (c) Ag<sub>50</sub>Cu<sub>50</sub>/Si and Ag<sub>50</sub>Cu<sub>50</sub>/Si MPs and (d) Cu/Si; and Cu/Si MPs, in a 0.5 mol L<sup>-1</sup> NaHCO<sub>3</sub> solution bubbled with CO<sub>2</sub> gas.  $\nu = 50\text{mV/s}$ .

In all cases the photocurrent plateau is attained at more elevated current densities for the 3D structures *vs.* flat substrates (with the exception of Cu/Si MPs), in line with the reduced optical losses with the MP structure (see **Figure 5b**).

In the presence of metal NPs, the *j/E* responses of the 3D electrodes appear systematically at less negative potentials than their flat counterparts, *i.e.*, a given current density can be achieved with Si MPs photocathodes versus flat photocathodes at a lower electrical energy input. For example, -0.56V for AgCu/Si MPs *vs.* -0.7V for AgCu/Si at -1.5 mA/cm<sup>2</sup> (see Table S2 for all values). This shows the potential interest of Si MPs for energy saving. However, this trend is not observed for bare Si electrodes (**Figure 6a**), as also observed by Lewis *et al.* [24]. In the present case, this is due to the higher level of surface defects of Si MPs which are generated during the MP fabrication process (plasma etching), which are actually eliminated during metal deposition as it is coupled to Si etching.

### 3.5 Ratiometric power saved

In order to quantify the energy conversion properties of the 3D photocathodes, the ratiometric saved power,  $\phi_{\text{saved}}$ , was determined. According to the work of Coridan *et al.*, it is defined as the ratio between the saved power,  $P_{\text{saved}}$ , at a given current value when using an illuminated photocathode versus its equivalent dark electrode, and the input solar power,  $P_{\text{input}}$  [34].

$$\left. \begin{aligned} \phi_{\text{saved}} &= \frac{P_{\text{saved}}(I)}{P_{\text{input}}} * 100 \\ P_{\text{saved}}(I) &= I * (E_{\text{dark}}(I) - E_{\text{light}}(I)) = I * \Delta V_{\text{saved}}(I) \end{aligned} \right\} \text{Eq. 1}$$

where  $E_{\text{light}}$  is the potential required to drive the reaction at a selected current value *I* for the illuminated photocathode and  $E_{\text{dark}}$  is the corresponding value for the dark electrode. This is a useful metric for solar energy conversion analysis of individual photoelectrodes in 3-electrode cells, without being affected by the presence of the counter electrode.

To perform these calculations, we recorded the *j/E* responses of metal dark electrodes chosen as Ag and Cu plates and Ag<sub>50</sub>Cu<sub>50</sub>/n<sup>++</sup>Si. **Figure 7** shows the *j/E* plots of Ag/Si MPs, Ag<sub>50</sub>Cu<sub>50</sub>/Si MPs and Cu/Si MPs at 0.2 Sun under CO<sub>2</sub>, together with those of the corresponding dark electrodes. For each photocathode  $\phi_{\text{saved}}$  is calculated at the point of maximum saved power,  $P_{\text{max}}$  (insets).

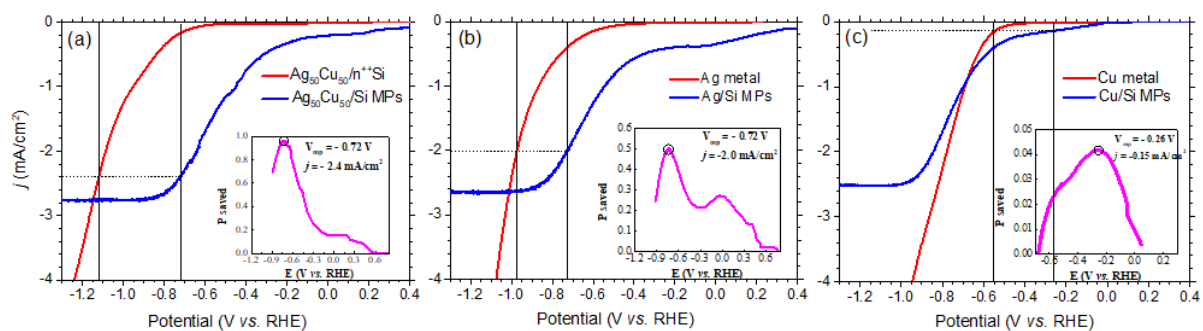


Figure 7. Polarization curves for (a) Ag metal vs. Ag/Si MPs; (b) Ag<sub>50</sub>Cu<sub>50</sub>/n<sup>++</sup>Si vs. Ag<sub>50</sub>Cu<sub>50</sub>/Si MPs and (c) Cu metal vs. Cu/Si MPs used to calculate power saving efficiency. Inset: Power saved (calculated from Eq.1) at each potential applied (E vs. RHE).  $V_{mp}$  and  $j$  on the insets correspond to the potential gain ( $E_{dark}-E_{light}$ ) and the corresponding photocurrent at the maximum power saved. Other conditions as in **Figure 6**.

The ratiometric saved power are 4.7% for Ag<sub>50</sub>Cu<sub>50</sub>/Si MPs, 2.5% for Ag/Si MPs and 0.2% for Cu/Si MPs. Thus, Ag<sub>50</sub>Cu<sub>50</sub>/Si MPs distinguish itself as the most efficient photoelectrode for solar energy conversion among the three considered, with ~5% of the  $P_{\text{saved}}$  resulting from solar energy conversion. It is important to note that a ratiometric saved power of 5% under 0.2 sun is a significant value for a Si photocathode based only on a p-Si/electrolyte junction. An equivalent flat Si/Ag<sub>50</sub>Cu<sub>50</sub> flat photocathode has been reported to have a ratiometric saved power of c.a. 3% <sup>[19]</sup>. As already observed for flat supports, the Cu metallized Si MPs photocathode has the lowest energy conversion efficiency. We believe that this poor performance with Cu is related to the catalyst degradation (Cu NPs detachment) during photoelectrolysis, which is accentuated between the Si MPs, due to their higher developed surface area and the reduced volume between the MPs, as explained in section 3.8.

$P_{\text{saved}}$  is related to the gain in potential (at the maximum power point) with a photocathode versus a dark electrode. Dividing  $P_{\text{saved}}$  by the power consumed by the dark electrode,  $P_{\text{dark}}$ , gives the actual electrical power gained. In our case,  $P_{\text{saved}}/P_{\text{dark}}$  is 26% for Ag and 36% for Ag<sub>50</sub>Cu<sub>50</sub>.

### 3.6 Influence of the bimetallic composition on the PEC-response

An advantage of bimetallic deposition by MACE over other deposition techniques, such as sputtering or electrodeposition, is that it allows obtaining well-defined NPs with a composition that can be easily tuned (by simply adjusting the ratio of metal precursors) over the whole range of atomic compositions. Thus, it enables the systematic study of the influence of the catalyst composition on specific observables.

Accordingly, we studied the influence of the bimetallic composition on the PEC response (at 0.2 sun under CO<sub>2</sub>), together with that of bare Si MPs as a reference, as shown in **Figure 8a**.

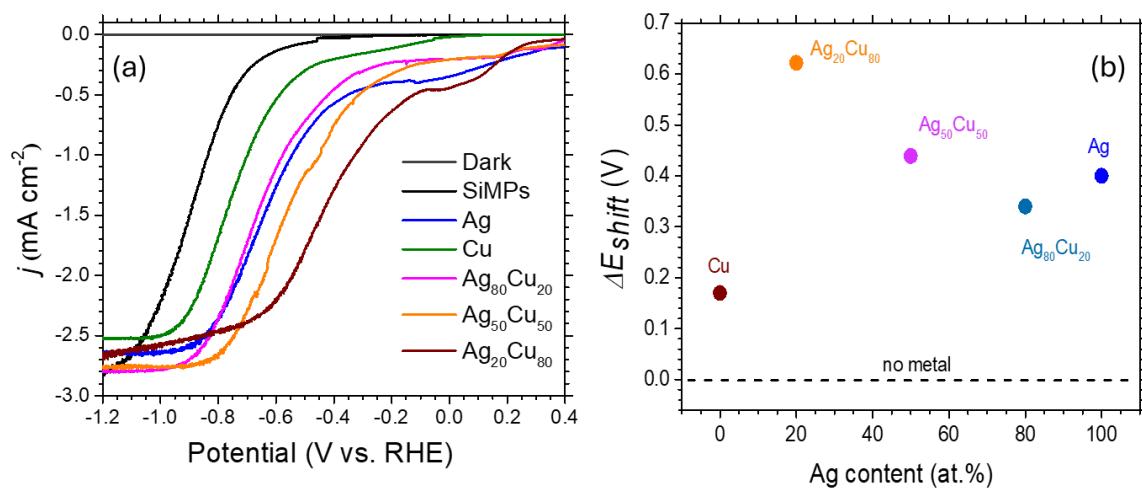


Figure 8. (a) Comparison of the  $j/E$  responses at 0.2 sun of  $Ag_xCu_{100-x}/Si$  MPs and Si MPs photoelectrodes in a  $0.5 \text{ mol L}^{-1} \text{ NaHCO}_3$  solution bubbled with  $\text{CO}_2$  gas.  $\nu = 50 \text{ mV/s}$ ; (b) corresponding potential shifts (at  $J_{ph} = -0.5 \text{ mA cm}^{-2}$ ) vs. bare Si MPs (no metal).

A clear influence of the bimetallic composition on the position of the PEC responses is revealed from this figure, with Ag<sub>20</sub>Cu<sub>80</sub>/Si MPs being the most favorable catalyst in terms of photocurrent and overvoltage. **Figure 8b** shows the potential shift versus bare Si MPs at a current density of -0.5 mA cm<sup>-2</sup> (selected to avoid the contribution of native metal oxide reduction observed at low cathodic potentials). A synergy between the two metals in terms of reduced overvoltage is observed from Ag<sub>50</sub>Cu<sub>50</sub> (+50 mV vs. pure Ag and 440 mV vs. bare Si MPs) to Ag<sub>20</sub>Cu<sub>80</sub> with the highest shift (+220 mV vs. pure Ag and +600 mV vs. Si MPs). The gain in potential from adding 20 at% Ag to Cu is striking (+450 mV).

It is important to highlight that the bimetallic NPs synthesized in this work have a phase separated crystalline structure with Ag and Cu intermixed nanograins (also called immiscible solid solution<sup>[35-37]</sup>) as mentioned in Section 3.2, which impacts the catalytic activity and selectivity, and hence the energy conversion properties of the 3D photocathode. It is possible that AgCu NPs with a different distribution (*e.g.*, core shell or Janus structures) present a different trend for the potential shift. A figure showing a comparison of the voltammograms obtained under Ar and CO<sub>2</sub> atmospheres is given in the SI (Figure S8). The electrochemical responses are not significantly different, suggesting that CO<sub>2</sub>RR and HER occur at similar potentials. Therefore, product identification is required to study the selectivity of the bimetallic catalysts.

### 3.7 PEC-CO<sub>2</sub>RR product analysis

Electrolysis coupled to gas chromatography (GC) under 1 sun illumination was used for product detection. **Figure 9** shows the faradaic efficiencies (FE) obtained with the different Si MPs photocathodes: bare and coated with Ag, Cu, Ag<sub>50</sub>Cu<sub>50</sub> and Ag<sub>20</sub>Cu<sub>80</sub> (**Figure 9a-e**, respectively). Figure S9 in the SI shows the corresponding chronoamperograms. A fixed potential of -0.87 vs. RHE was used based on previous studies.

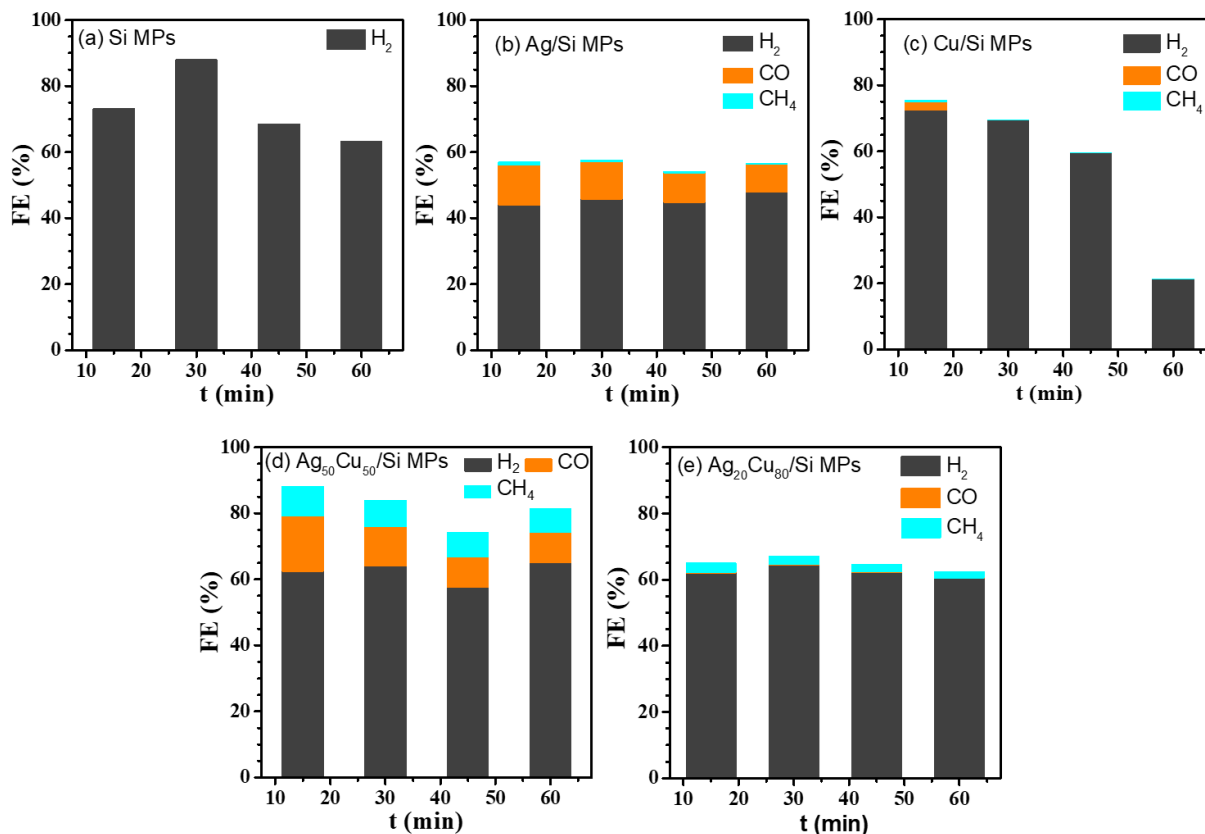


Figure 9. FE of gaseous products formed during photoelectrolysis ( $\text{H}_2$ ,  $\text{CO}$ ,  $\text{CH}_4$ ) at  $-0.87$  V vs. RHE in a  $0.5 \text{ mol L}^{-1}$   $\text{NaHCO}_3$  solution bubbled with  $\text{CO}_2$  gas. GC measurements every 15 min for 1 h; (a) bare Si MPs; (b) Ag/Si MPs; (c) Cu/Si MPs; (d)  $\text{Ag}_{50}\text{Cu}_{50}$ /Si MPs; and (e)  $\text{Ag}_{20}\text{Cu}_{80}$ /Si MPs.

As expected, the bare Si MPs produced only  $\text{H}_2$  (**Figure 9a**). The Ag/Si MPs photocathode produces  $\text{CO}$  with a maximum FE of 12.1% and a very small amount of  $\text{CH}_4$  ( $\text{FE} < 1\%$ ) (**Figure 9b**). In the case of Cu/Si MPs,  $\text{H}_2$  is the main product, with  $\text{CO}$  during the first few minutes, and traces of  $\text{CH}_4$  throughout the experiment (**Figure 9c**). The bimetallic Si MPs photocathodes, especially with  $\text{Ag}_{50}\text{Cu}_{50}$ , reduce  $\text{CO}_2$  to  $\text{CO}$  and  $\text{CH}_4$  throughout the experiment, with a maximum FE of 16.7% and 9%, respectively (**Figure 9d-e**). The most interesting bimetallic composition from the energy saving point of view (section 3.5),  $\text{Ag}_{20}\text{Cu}_{80}$ /Si MPs, selectively produces  $\text{CH}_4$ , but with FE values not higher than 5%. Finally, between  $\text{Ag}_{50}\text{Cu}_{50}$  and  $\text{Ag}_{20}\text{Cu}_{80}$ , the former is more efficient in terms of total  $\text{CO}_2$  conversion. These results demonstrate the ability of the bimetallic catalysts in directing the PEC- $\text{CO}_2$  selectivity towards the energy dense product  $\text{CH}_4$ .

An enhanced selectivity for  $\text{CH}_4$  production has been reported with bimetallic catalysts and is often attributed to phase-separated structures with highly intermixed nanograins.<sup>[15,37]</sup> The proposed mechanism involves Ag sites facilitating the initial  $\text{CO}_2$ -to- $\text{CO}$  conversion,

creating a CO-enriched environment that Cu sites utilize for further reduction into  $C_1$  and  $C_2$  products. Once CO is produced, the selectivity between  $C_1$  and  $C_{2+}$  products (such as  $CH_4$  or  $C_2H_4$ ) is influenced by the bimetallic crystal structure. AgCu nanoparticles with segregated domains mainly produce  $C_2H_4$ , as C-C coupling occurs at adjacent Cu sites, while catalysts with more intermixed Ag and Cu domains favor  $CH_4$  production. DFT calculations suggest that both products share a common pathway involving  $*COH$  as intermediate, with the outcome being  $CH_4$  or  $C_2H_4$  depending on the catalyst's ability to adsorb H or CO and the length scale to which the metal mixture promotes C-C coupling.

If we compare the FE values obtained for  $Ag_{50}Cu_{50}/SiMPs$  in this work with a homologous flat photocathode<sup>[19]</sup> (Figure S10) we observed an inversion of the catalytic activity towards the products CO and  $CH_4$ : in the same experimental conditions,  $Ag_{50}Cu_{50}/p-Si$  provides CO/ $CH_4$  in a ratio  $\sim 0.3$  (18.2 % FE for  $CH_4$  and 5.2% for CO) while  $Ag_{50}Cu_{50}/p-Si$  MPs provides CO/ $CH_4$  at  $\sim 1.8$  (16.7% FE for CO and 9% for  $CH_4$ ). We believe this is due to the richer Ag content of the bimetallic NPs in these samples, specially at the top of the Si MPs (see SEM-EDX analysis in **Figure 4** and TEM-EDX Figure S7), which favors CO detachment from Ag sites over stabilization and hydrogenation in concomitant Cu sites. Only  $CH_4$  is observed for  $Ag_{20}Cu_{80}/SiMPs$  (no CO production), which can be explained by the richer Cu environment in this composition (observed composition  $Ag_{36}Cu_{64}$  by TEM-EDX) which favors CO spillover from Ag sites towards Cu sites, and  $CH_4$  production. A similar behavior is observed for  $Ag_{20}Cu_{80}$  on flat supports (Figure S10). The interest of a NP synthesis method allowing easy tuning of the bimetallic composition can be discerned from these results.

Despite the potentiality of the presented photocathodes for PEC- $CO_2RR$ , the majority product is still  $H_2$ . Indeed,  $H_2$  is obtained in higher amounts with Si MPs *vs.* flat Si supports, especially for Cu/Si MPs. Thus, although Si MPs-based photocathodes perform better than flat substrates for energy conversion, they appear to be less efficient for  $CO_2RR$ . The origin of this behavior will be investigated in the next section.

### 3.8 Catalyst stability evaluation

We performed several tests to investigate the stability of the catalysts. **Figure 10** shows SEM images of  $Ag_{50}Cu_{50}/Si$  MPs (panel (a)) and  $Ag_{20}Cu_{80}/Si$  MPs (panel (b)) after 1 h of photoelectrolysis, together with the corresponding XPS spectra.

SEM images revealed a severe loss of metal NPs after PEC measurements. The coverage decreased significantly (almost no particles were found at the bottom, see Fig. S11 in the SI) and the remaining NPs aggregated into dense clusters. The loss was more acute for the monometallic photocathodes, especially Cu/Si MPs (Fig. S12), for which no metal NPs were observed after electrolysis. The agglomeration and detachment of metal NPs leaves free Si surfaces for HER, which is the reason for the lower CO<sub>2</sub>RR efficiency. Cu NP instability leading to a lower selectivity for CO<sub>2</sub>RR is a well-known problem and many efforts are being devoted to overcome it<sup>[25,26]</sup>. Nevertheless, it is important to emphasize that the bimetallic photocathodes are significantly more resistant to catalyst degradation than their monometallic counterparts. Thus, the bimetallic interactions stabilize the catalyst up to a certain extent.

We hypothesized that the stronger degradation of the catalyst on Si MPs than on flat Si is actually a consequence of its higher activity, since it is accompanied by an increase in gas production from the CO<sub>2</sub>RR and HER. The gas bubbles that develop between the packed arrays of MPs should generate important frictional forces that favor NP detachment. The advantage of Si MPs to have a large surface area and thus a higher catalytic activity becomes a problem to retain small metal NPs bound to their walls by electrostatic forces.

The surface composition and chemical state for the Ag<sub>50</sub>Cu<sub>50</sub>/Si MPs and Ag<sub>20</sub>Cu<sub>80</sub>/Si MPs photocathodes after 1 h of photoelectrolysis were evaluated by XPS. The peaks of Ag 3d<sub>5/2</sub> and Cu 2p<sub>3/2</sub> core-level emission spectra along with their doublets (Ag 3d<sub>3/2</sub> and Cu 2p<sub>1/2</sub>) are shown in **Figure 10** (panels (a) and (b), respectively). The peaks at 367.9 and 373.9 eV correspond to Ag<sup>0</sup> 3d (Ag 3d<sub>5/2</sub> and Ag 3d<sub>3/2</sub>). No oxide peak (Ag-O) was observed. The metallic Cu 2p core-level peaks were centered at 932.2 eV and 952.1 eV. Oxidized Cu (Cu-O) peaks at 934.05 eV and 953.9 eV were also observed. The compositional analysis shows that the remaining (agglomerated) NPs have a Ag rich surface. For Ag<sub>50</sub>Cu<sub>50</sub>, the surface is actually Ag<sub>60</sub>Cu<sub>40</sub>. A larger change is observed for Ag<sub>20</sub>Cu<sub>80</sub>, with Ag<sub>93</sub>Cu<sub>7</sub> on the surface after PEC. These values are average due to the compositional gradient existing along the MPs, which cannot be distinguished by XPS. However, the presence of some Cu remaining after PEC nevertheless indicates that the AgCu bimetallic helps to prevent total Cu loss.

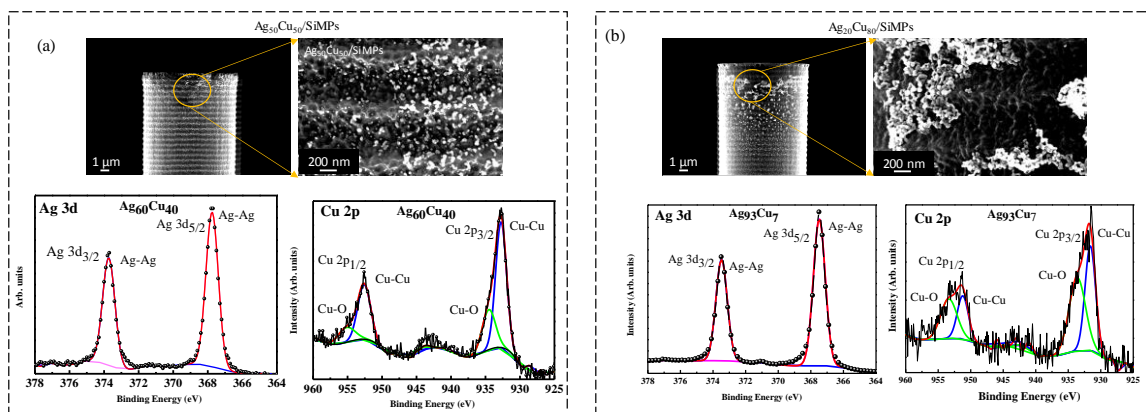


Figure 10. SEM images and XPS spectra of bimetallic NPs on MPs based photocathode after 1 h of photoelectrolysis at  $-0.87\ \text{V vs. RHE}$ ; (a)  $\text{Ag}_{50}\text{Cu}_{50}/\text{p-Si}$  MPs; (b)  $\text{Ag}_{20}\text{Cu}_{80}/\text{p-Si}$  MPs. Ag 3d and Cu 2p XPS core-level experimental spectra are plotted as black circles and the corresponding peak analysis as blue, green, and red lines. The surface compositions measured by XPS are indicated.

## 4 Conclusion and Perspectives

Overall, we have demonstrated the feasibility of MACE as a method to deposit bimetallic Ag<sub>x</sub>Cu<sub>100-x</sub> NPs in 3D electrodes, specifically Si MPs. These macrostructured substrates are promising for driving PEC reactions (CO<sub>2</sub>RR in this case) from an energy saving point of view compared to homologous flat photocathodes, as indicated by their enhanced light trapping capabilities, higher photocurrent density at a given overpotential, and superior power savings. In addition, bimetallic coated photocathodes are more efficient in energy conversion than monometallic ones and more selective in CO<sub>2</sub> reduction towards high energy density products (in this case CH<sub>4</sub>). The compositions that provide the largest gain in potential and resistance to degradation (Ag<sub>20</sub>Cu<sub>80</sub> and Ag<sub>50</sub>Cu<sub>50</sub>, respectively) have been identified. These novel materials have great potential for efficient light-driven CO<sub>2</sub> conversion.

The proposed deposition method allows a fairly good control of the bimetallic composition and a bimetallic coating all along the sample. Nevertheless, it shows an important dependence on the ion supply to the 3D surfaces by diffusion, which generates gradients in the bimetallic coatings, with a high NP density in the middle and upper part of the pillars compared to the bottom. We are currently investigating the impact of bimetallic deposition under dynamic conditions, *i.e.*, with constant agitation of the precursor solutions at different sweep rates for forced convection, with encouraging results.

Although the 3D photocathodes show high potential to drive PEC reactions with a lower external energy input compared to flat surfaces, the stability of the catalysts is negatively affected due to the intense gas evolution between the MPs combined with the intrinsic instability of Cu-based nanoelectrocatalysts. Current efforts are devoted to developing methods to prevent catalyst detachment, from simply increasing the catalyst loading (as in the work of Lewis *et al.*<sup>[24]</sup> for pure Cu NPs) without preventing light absorption, to developing advanced protective layers by area selective atomic layer deposition.

This is the first time that Si MPs coated with bimetallic NPs have been applied to the PEC-CO<sub>2</sub>RR. We believe that the findings presented in this work will be a useful guide for the development of easily scalable, more efficient light-driven systems for CO<sub>2</sub>RR based on metal-coated 3D Si substrates.

## 5 Acknowledgements

This work was supported by the French National Research Agency (Grant ANR JCJC SIROCCO 2022-2024) and the ISite Project Future (Exploratory Project EVOLVE 2021-2022, Gustave Eiffel40 University). H. A. Chaliyawala acknowledges CNRS for a postdoctoral fellowship (2022–2024). The authors also acknowledge R. Pires Brazuna for technical assistance with the SEM/EDX instrument (microscopy facilities of the East-Paris Institute of Chemistry and Materials). Finally, the authors acknowledge the support of the Centre National de la Recherche Scientifique (CNRS) for providing the central facilities to carry out this work.

## 6 References

- [1] K. Calvin, D. Dasgupta, G. Krinner, A. Mukherji, P. W. Thorne, C. Trisos, J. Romero, P. Aldunce, K. Barrett, G. Blanco, W. W. L. Cheung, S. Connors, F. Denton, A. Diongue-Niang, D. Dodman, M. Garschagen, O. Geden, B. Hayward, C. Jones, F. Jotzo, T. Krug, R. Lasco, Y.-Y. Lee, V. Masson-Delmotte, M. Meinshausen, K. Mintenbeck, A. Mokssit, F. E. L. Otto, M. Pathak, A. Pirani, E. Poloczanska, H.-O. Pörtner, A. Revi, D. C. Roberts, J. Roy, A. C. Ruane, J. Skea, P. R. Shukla, R. Slade, A. Slangen, Y. Sokona, A. A. Sörensson, M. Tignor, D. Van Vuuren, Y.-M. Wei, H. Winkler, P. Zhai, Z. Zommers, J.-C. Hourcade, F. X. Johnson, S. Pachauri, N. P. Simpson, C. Singh, A. Thomas, E. Totin, A. Alegría, K. Armour, B. Bednar-Friedl, K. Blok, G. Cissé, F. Dentener, S. Eriksen, E. Fischer, G. Garner, C. Guivarch, M. Haasnoot, G. Hansen, M. Hauser, E. Hawkins, T. Hermans, R. Kopp, N. Leprince-Ringuet, J. Lewis, D. Ley, C. Ludden, L. Niamir, Z. Nicholls, S. Some, S. Szopa, B. Trewin, K.-I. Van Der Wijst, G. Winter, M. Witting, A. Birt, M. Ha, P. Arias, M. Bustamante, I. Elgizouli, G. Flato, M. Howden, C. Méndez-Vallejo, J. J. Pereira, R. Pichs-Madruga, S. K. Rose, Y. Saheb, R. Sánchez Rodríguez, D. Ürge-Vorsatz, C. Xiao, N. Yassaa, J. Romero, J. Kim, E. F. Haites, Y. Jung, R. Stavins, A. Birt, M. Ha, D. J. A. Orendain, L. Ignon, S. Park, Y. Park, A. Reisinger, D. Cammaramo, A. Fischlin, J. S. Fuglestvedt, G. Hansen, C. Ludden, V. Masson-Delmotte, J. B. R. Matthews, K. Mintenbeck, A. Pirani, E. Poloczanska, N. Leprince-Ringuet, C. Péan, *IPCC, 2023: Climate Change 2023: Synthesis Report. Contribution of Working Groups I, II and III to the Sixth Assessment Report of the Intergovernmental Panel on Climate Change [Core Writing Team, H. Lee and J. Romero (Eds.)]. IPCC, Geneva, Switzerland., Intergovernmental Panel On Climate Change, 2023.*
- [2] S. M. Grodsky, *One Earth* **2021**, *4*, 924–926.
- [3] B. Zhou, J. Li, X. Dong, L. Yao, *Sci. China Chem.* **2023**, DOI 10.1007/s11426-022-1508-y.
- [4] P. M. Rajaita, S. Hajra, K. Mistewicz, S. Panda, M. Sahu, D. Dubal, Y. Yamauchi, H. J. Kim, *J. Mater. Chem. A* **2022**, *10*, 15906–15931.
- [5] A. Kumar, V. Hasija, A. Sudhaik, P. Raizada, Q. Van Le, P. Singh, T.-H. Pham, T. Kim, S. Ghotekar, V.-H. Nguyen, *Chemical Engineering Journal* **2022**, *430*, 133031.

- [6] K. Li, J. Ge, E. Li, Z. Li, H. Wang, Y. Wang, Y. Zhou, J.-J. Zhu, *EES. Catal.* **2023**, *1*, 687–694.
- [7] T. Liu, L. Liu, Z.-Y. Guo, D.-F. Liu, L.-L. Jiang, K. M. Liew, W.-W. Li, *Energy Reviews* **2025**, *4*, 100110.
- [8] K. Xu, Q. Zhang, X. Zhou, M. Zhu, H. Chen, *Nanomaterials* **2023**, *13*, 1683.
- [9] M. Li, Q. Wang, Y. He, Y. Wang, K. Wang, P. Tsiakaras, S. Song, *Coordination Chemistry Reviews* **2023**, *495*, 215373.
- [10] J. Yu, X. Hao, L. Mu, W. Shi, G. She, *Chemistry – A European Journal* **n.d.**, *n/a*, e202303552.
- [11] J. Kang, W. He, K. Wang, Y. Chen, Y. Liu, Y. Li, W. Li, *Chem. Commun.* **2024**, *60*, 6039–6042.
- [12] X.-Y. Li, Z.-L. Zhu, F. W. Dagnaw, J.-R. Yu, Z.-X. Wu, Y.-J. Chen, M.-H. Zhou, T. Wang, Q.-X. Tong, J.-X. Jian, *Nat Commun* **2024**, *15*, 5882.
- [13] W. Zhuang, M. Kan, T. Meng, J. Zhang, *Sci. China Chem.* **2024**, *67*, 1904–1921.
- [14] D. Seo, A. Ma, T. Kwon, K. M. Nam, *Inorg. Chem. Front.* **2024**, *11*, 998–1018.
- [15] P. Guo, K. Liu, X. Liu, R. Liu, Z. Yin, *Energy Fuels* **2024**, *38*, 5659–5675.
- [16] L. Liu, A. Corma, *Chem. Rev.* **2023**, *123*, 4855–4933.
- [17] O. Zoubir, L. Atourki, H. A. Ahsaine, A. BaQais, *RSC Adv.* **2022**, *12*, 30056–30075.
- [18] Y. Jia, F. Li, K. Fan, L. Sun, *Advanced Powder Materials* **2022**, *1*, 100012.
- [19] H. A. Chaliyawala, S. Bastide, D. Muller-Bouvet, C. Pichon, K. Bah, A. Djoumoi, F. Marty, T. Bourouina, E. Torralba, *ACS Appl. Energy Mater.* **2023**, *6*, 8397–8409.
- [20] E. Torralba, S. L. Gall, H. Chaliyawala, É. Chopard, Z. A. Rahhou, D. Muller-Bouvet, C. Cachet-Vivier, S. Bastide, *Applied Surface Science* **2024**, *649*, 159117.
- [21] B. Shang, F. Zhao, S. Suo, Y. Gao, C. Sheehan, S. Jeon, J. Li, C. L. Rooney, O. Leitner, L. Xiao, H. Fan, M. Elimelech, L. Wang, G. J. Meyer, E. A. Stach, T. E. Mallouk, T. Lian, H. Wang, *J. Am. Chem. Soc.* **2024**, *146*, 2267–2274.
- [22] S. Yalamanchili, P. A. Kempler, K. M. Papadantonakis, H. A. Atwater, N. S. Lewis, *Sustainable Energy Fuels* **2019**, *3*, 2227–2236.
- [23] E. L. Warren, H. A. Atwater, N. S. Lewis, *J. Phys. Chem. C* **2014**, *118*, 747–759.
- [24] P. A. Kempler, M. H. Richter, W.-H. Cheng, B. S. Brunschwig, N. S. Lewis, *ACS Energy Lett.* **2020**, *5*, 2528–2534.
- [25] P. Wilde, P. B. O’Mara, J. R. C. Junqueira, T. Tarnev, T. M. Benedetti, C. Andronescu, Y.-T. Chen, R. D. Tilley, W. Schuhmann, J. J. Gooding, *Chem. Sci.* **2021**, *12*, 4028–4033.
- [26] S. Popović, M. Smiljanić, P. Jovanović, J. Vavra, R. Buonsanti, N. Hodnik, *Angew. Chem. Int. Ed.* **2020**, *59*, 14736–14746.
- [27] I. Roh, S. Yu, C.-K. Lin, S. Louisia, S. Cestellos-Blanco, P. Yang, *J. Am. Chem. Soc.* **2022**, *144*, 8002–8006.
- [28] Y. Wang, J. G. Limon-Petersen, R. G. Compton, *J. Electroanal. Chem.* **2011**, *652*, 13–17.
- [29] Q. Cao, Z. Shao, D. K. Hensley, N. V. Lavrik, B. J. Venton, *Langmuir* **2021**, *37*, 2667–2676.
- [30] I. Pana, A. C. Parau, M. Dinu, A. E. Kiss, L. R. Constantin, C. Vitelaru, *Metals* **2022**, *12*, 262.
- [31] J. He, C. Janáky, *ACS Energy Letters* **2020**, *5*, 1996–2014.
- [32] C. J. P. Allen J. Bard, Martin Stratmann, Fritz Scholz, *Encyclopedia of Electrochemistry: Inorganic Electrochemistry*, **2006**.

- [33] N. S. L. Ming X. Tan, Paul E Laibinis, Sonbinh T. Nguyen, Janet M. Kesselman, Colby E. Stanton, *Principles and Applications of Semiconductor Photoelectrochemistry*, Wiley, **1994**.
- [34] R. H. Coridan, A. C. Nielander, S. A. Francis, M. T. McDowell, V. Dix, S. M. Chatman, N. S. Lewis, *Energy Environ. Sci.* **2015**, *8*, 2886–2901.
- [35] J. Huang, M. Mensi, E. Oveisi, V. Mantella, R. Buonsanti, *J. Am. Chem. Soc.* **2019**, *141*, 2490–2499.
- [36] C. Yang, B. H. Ko, S. Hwang, Z. Liu, Y. Yao, W. Luc, M. Cui, A. S. Malkani, T. Li, X. Wang, J. Dai, B. Xu, G. Wang, D. Su, F. Jiao, L. Hu, *Sci. Adv.* **2020**, *6*, eaaz6844.
- [37] C. Choi, J. Cai, C. Lee, H. M. Lee, M. Xu, Y. Huang, *Nano Res.* **2021**, *14*, 3497–3501.

**Keywords:** electron transfer, metal assisted chemical etching, bimetallic nanoparticles, solar-to-chemical conversion, carbon dioxide utilization.